Chemical Physics Letters 815 (2023) 140362

Contents lists available at ScienceDirect

Chemical Physics Letters

journal homepage: www.elsevier.com/locate/cplett

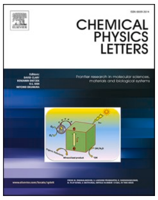

Research paper

A comparison of the electrochemical performance of graphitized coal prepared by high-temperature heating and flash Joule heating as an anode material for lithium and potassium ion batteries

A.M.A. Mohamed [a,b,*], Shu Dong [a], Maged Elhefnawey [c], Guangsheng Dong [a], Yinyi Gao [a], Kai Zhu [a], Dianxue Cao [a,*]

[a] *Key Laboratory of Superlight Materials and Surface Technology, College of Material Science and Chemical Engineering, Harbin Engineering University, Harbin 150001, China*
[b] *Department of Physics, Faculty of Education, University of Dongola, Sudan*
[c] *Department of Mechanical Engineering, Faculty of Engineering, Kafrelsheikh University, Kafrel-sheikh 33156, Egypt*

ARTICLE INFO

Keywords:
Lithium ion batteries
Potassium ion batteries
High-temperature heating
Flash Joule heating
Graphitized coal

ABSTRACT

Natural graphite, commonly used in energy storage applications such as the battery industry, is marked as a supply-risk material due to the elevated demand and limited resources. The synthetic graphite process is inefficient, so there is a highly required for alternative methods of making graphite as anode material. In this study, we report two efficient methods for catalytic graphitization of coal using high-temperature heating and flash Joule heating (FJH). Using both methods, the structure and morphology characterizations have demonstrated the successful structural conversion of coal from an amorphous structure into a crystalline structure. When the obtained graphitized coal samples via the high-temperature heating method (HTC) and via the FJH method (FHC) were used as anodes for lithium-ion batteries (LIBs) and potassium-ion batteries (PIBs), the HTC and FHC presented outstanding rate capability and remarkable stable cycling performance. The HTC and FHC anodes delivered initial charge capacities of 322.5 and 321.3 mAh·g^{-1}, respectively, at a current density of 0.1C. for LIBs. When used as anodes in PIBs, the HTC and FHC delivered initial charge capacities of 265.4 and 262.2 mAh·g^{-1} at 0.1C current density. These results make the HTC and FHC promising materials for developing energy storage applications. Therefore, this work exploited the low price of coal and its abundant reserves, combined with the FJH technique, which is an effective method for saving energy and time, to produce high-quality graphitized coal materials, which can make this process green and economically attractive.

1. Introduction

To address the threat of depletion of fossil fuel resources, increasing crude oil prices, an explosive population together with economic growth, global warming, and a shortage of energy resources [1,2]. It is necessary to develop storage devices like fuel cells, supercapacitors, and batteries [3]. This could ensure the best utilization of renewable energy sources like wind and solar [4], which leads to the fulfillment of the needs of modern society. Among several energy storage technologies, rechargeable lithium-ion batteries (LIBs) are thought to address the above issues [5]. Due to their advantages, such as high energy density, longer cycling stability, and no memory effect, LIBs have been dominating the small-format battery market [6,7]. LIBs have been used in various electronic devices since their market introduction 30 years ago, including mobile phones, laptop computers, digital cameras, and even hybrid and electric vehicles [8–10]. However, because of the uneven global distribution and limited resources of lithium, with its rising prices, the industry of LIBs is becoming more expensive, which further limits its application in future large-scale energy storage systems [11].

Therefore, it is more critical to decrease the usage of rare elements in storage batteries and search for alternative battery systems based on earth-abundant elements. Hence, it has encouraged the field of alternative ion batteries using abundant earth metals, such as calcium-ion, magnesium-ion, aluminum-ion, sodium-ion, and potassium-ion

---

* Corresponding authors at: Key Laboratory of Superlight Materials and Surface Technology, College of Material Science and Chemical Engineering, Harbin Engineering University, Harbin 150001, China (A.M.A.Mohamed, D.Cao).

E-mail addresses: abdallamohamed@hrbeu.edu.cn (A.M.A. Mohamed), caodianxue@hrbeu.edu.cn (D. Cao).

https://doi.org/10.1016/j.cplett.2023.140362
Received 4 October 2022; Received in revised form 17 January 2023; Accepted 7 February 2023

[12–15]. Recently, sodium-ion batteries (SIBs) and potassium-ion batteries (PIBs) have attracted considerable attention. They are regarded as alternative storage technologies for LIBs due to their low cost and abundant resources of Na and K compared with Li. Additionally, the electrochemical properties of Na and K are similar to Li [16]. Thus, SIBs and PIBs are expected to be promising energy storage systems. Sodium has a higher negative redox potential with a specification (−2.71 V vs standard hydrogen electrode (SHE)) and a larger ionic radius compared to Li^+, which causes a significant volume expansion and large polarization [17]. Furthermore, by the density functional theory, sodium and graphite can hardly form a stable intercalation compound (they only form NaC_{64}) [18], resulting in lower reversible capacities and poor cycle life, which inhibits the SIBs' commercial application [19]. In contrast, potassium has a lower negative redox potential (−2.93 V vs SHE) than sodium and higher ionic conductivity in electrolytes than in Li^+ and Na^+ [20]. This is due to the smaller solvated potassium ions that lead to a weak interaction with the solvent molecules during the solvation process [21]. This contributes to the high ionic conductivity of PIBs so that ions can be quickly diffused. Furthermore, potassium may form KC_8 with graphite and undergo reversible insertion and extraction; thus, PIBs are more promising options for LIBs than SIBs [22]. However, the commercial applicability of PIBs is severely limited due to their poor cycling stability and inferior rate performance as a result of the larger radius of the K^+ (1.38 Å) than that of Na^+ (1.02 Å) and Li^+ (0.76 Å) [23]. As a result, its insertion/ deinsertion in electrode materials will cause substantial volumetric deformation, making them prone to performance decay and structural degradation [24]. Consequently, exploring more suitable PIBs anodes for high capacity and cyclability is urgently needed.

Typically, the commercial success of graphite in LIBs has stimulated researchers to use it as a PIBs anode. The first investigation exhibited a high reversible capacity of 273 $mAh{\cdot}g^{-1}$ at a minimal current density of C/40 through the formation of the KC_8 intercalation compound [25]. Nevertheless, its capacity decreased dramatically when the current density increased, with just 80 $mAh{\cdot}g^{-1}$ retained at 1C. Meanwhile, after 50 cycles, the graphite showed a lower cycling performance with retention of around 50 %. The lower cycling stability and poor rate performance can be associated with graphite's dramatic volume expansion due to the large ionic radius of K^+ [23]. So, manufacturing low-cost and high-performance carbon anodes for PIBs is urgently needed to solve this problem. Apart from graphite, amorphous carbon, specifically hard carbon (known as non-graphitic carbon), could be a promising candidate for PIBs anode materials because of its relatively low surface area, larger interlayer spacing, hierarchical porous structures, and rich defects [26]. As a high-quality carbon source, coal has many advantages compared with other carbon sources. This includes a high-quality carbon skeleton structure, an abundant energy source, a low cost, widespread distribution, high carbon content, ease of acquisition, and a stable environment [27]. Thus, coal has attracted considerable attention as a vital raw resource for preparing functional carbon materials on a large scale [28], enabling fossil fuel usage at a high value-added level and significantly reducing production costs [27]. Recently, the electrochemical performance of coal-based carbon anodes for LIBs and SIBs has been promising [28]. However, the use of coal-based carbon anodes in PIBs has received little attention in the literature to the best of our knowledge.

The process of increasing the crystallinity of carbon is known as catalytic graphitization [29]. During this process, ungraphitized carbon becomes more ordered and crystallized by a chemical reaction between non-graphitic carbon and the metal or inorganic compound that constitutes the graphitization catalyst [30]. The catalyst is the most critical factor influencing the graphitization process of carbon; it can be divided into three types. Firstly, transition metals catalysts such as nickel (Ni), cobalt (Co), and iron (Fe); secondly, metallic compound catalysts such as Fe_2O_3, Cr_2O_3, and MnO_2 and thirdly, alloy catalysts such as P-Ni and Fe-Si alloys [31,32]. Ni is particularly effective among catalysts named above and has been generally used to obtain a graphitic structure with relatively high crystallinity. For example, Chen et al. [33] successfully obtained porous graphitized carbon from coal by adopting a low-temperature metal catalysis process by adding a $NiC_{l2}{\cdot}6H_2O$ catalyst. Destyorini et al. [34] generated graphitic carbon from amorphous carbon of coconut coir at 1300 °C using $NiC_{l2}{\cdot}6H_2O$-based catalytic graphitization. This method involves impregnating the amorphous carbon with a catalyst followed by a heat treatment in the furnace at temperatures between 700 and 1800 °C under an inert atmosphere for 1–6 h [35]. However, this method is very energy-intensive due to the utilization of such high temperatures, which severely limits its ability to scale up. In light of these considerations, a novel technique that can function at a lower cost of energy and time and with greater simplicity of preparation is needed. Regarding this, the flash Joule heating (FJH) method is considered a time and energy-saving and strong candidate for a traditional graphitization method. In the FJH technique, amorphous carbon powder is softly compressed between two electrodes inside a ceramic or quartz tube [36]. For outgassing to be more efficient, the system might be at atmospheric pressure or under a light vacuum (10 mm Hg) [37]. The electrodes may be made of graphite, copper, or any other conductive refractory material and are loosely fitted within the quartz tube to allow outgassing upon FJH [38]. The carbon source is heated to almost 3000 K in less than 100 ms by a high-voltage electric discharge from a capacitor bank, transforming the amorphous carbon into turbostratic flash graphene [35,36].

Based on the above considerations, the present work aims to use cleaned coal as an alternative to natural graphite and prepare it by catalytic graphitization using two methods; traditional high-temperature heating and the FJH. The electrochemical behavior of the obtained samples was evaluated as anode materials for LIBs and PIBs. HTC and FHC electrodes delivered initial reversible capacities of 322.5 and 321.3 $mAh{\cdot}g^{-1}$, respectively, at a current density of 0.1C for LIBs. For PIBs, the initial reversible capacities of HTC and FHC were 265.4 and 262.2 $mAh{\cdot}g^{-1}$, respectively, at a current density of 0.1C. In addition, both samples provide excellent rate capability and stable cycling performance as anode materials for LIBs and PIBs. The present study has the following benefits: (i) with the advantages of low cost and abundance, coal could be a promising alternative for natural graphite; (ii) due to the rising prices and limited resources of lithium, PIBs could be promising energy storage systems because of the abundance and cheap cost of potassium resources; and (iii) the obtained samples showed very similar electrochemical performance results for LIBs and PIBs, indicating that the FJH method is less expensive and environmentally friendly compared with the conventional heating method.

2. Experimental section:

2.1. Material synthesis:

The graphitized coal was prepared using two steps; carbonization followed by a catalytic activation and graphitization by high-temperature and the flash Joule heating (FJH) methods.

2.1.1. Carbonization at 600 °C

Due to its high carbon content, raw coal powder (RC), which has an amorphous structure, was used as a carbon source to prepare coal-based activated carbon. Before use, coal powder was sieved by using stainless steel (400 mesh) to obtain a smaller particle size instead of grinding to minimize the damage that can be caused to the primary structure of raw coal. Then, it was washed with deionized water and vacuum-dried for 24 h at 60 °C. The cleaned coal powder was carbonized in the tube furnace at 600 °C with a 5 °C min^{-1} heating rate and detained for 6 h under purity argon (99.99 %) flow, then collected after natural cooling. After that, in ethanol, nickel chloride was mixed with the carbonized coal powder with a ratio of 100 ml, 5 mmol, and 1 g, respectively, to dissolve the nickel catalyst and stirred for 1 h at 600 rpm. The Ni-impregnated carbon coal powder was obtained after drying for 24 h at

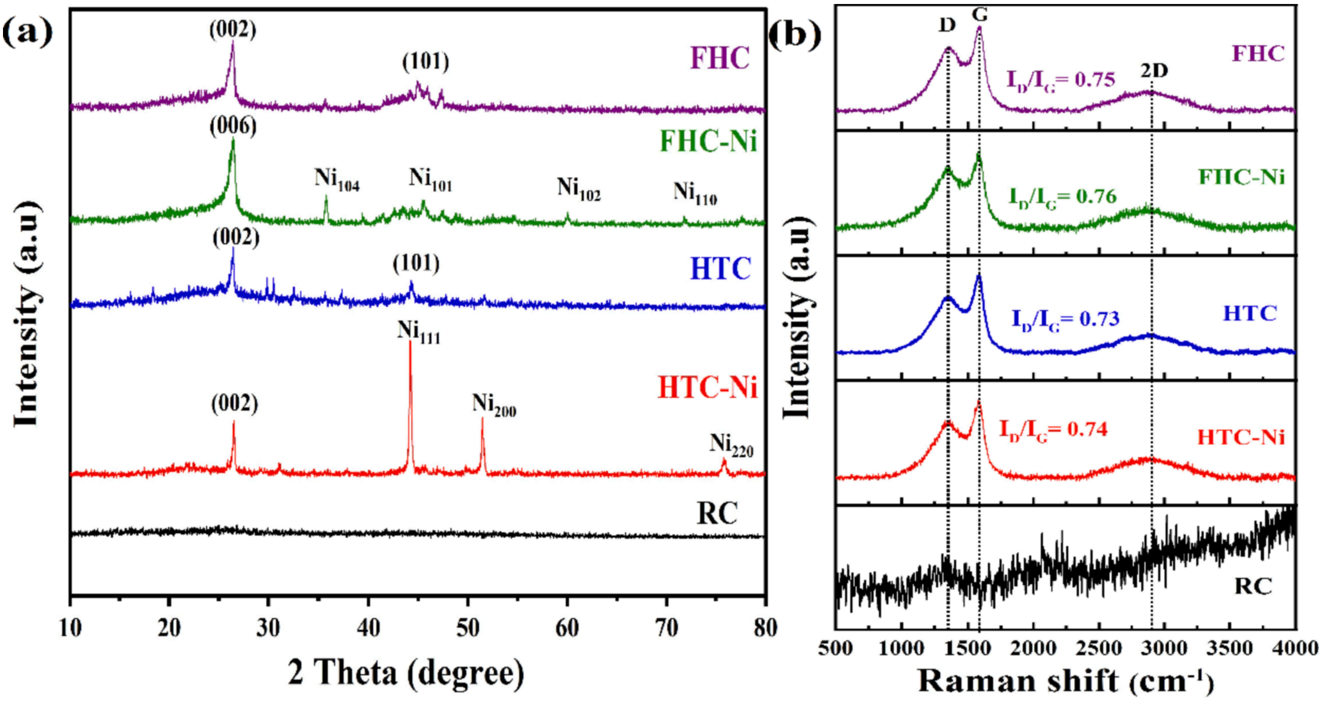

Fig. 1. (a) XRD patterns and (b) Raman spectra of raw coal and the prepared samples.

80 °C.

2.1.2. Graphitization at 1400 °C

A high-temperature furnace under an argon atmosphere (purity of 99.99 %) was used to conduct the catalytic graphitization treatment. In brief, carbon coal powder, obtained in the first step, was filled into the crucible of corundum and heated in a high-temperature furnace at 1400 °C using a 5 °C min^{-1} heating rate under Ar flow and held for 10 h. After the furnace was cooled down by the same heating rate to room temperature, the graphitized coal carbon was collected and washed using HCL acid to remove the Ni catalyst. Then, it was repeatedly washed with deionized water to ensure the total removal of the catalyst ions and HCL. Finally, graphitized coal material was obtained after desiccating at 60 °C for 24 h under vacuum pressure and was denoted as HTC.

2.1.3. FJH system and synthesis process:

In the flash-heated process, conducting additive of carbon black and carbon coal powder with a (10:90) weight ratio was mixed by grinding using a mortar and pestle. Then 100 mg of mixed powder was accurately weighed and loaded into a quartz tube (inner diameter: 4 mm, tube thickness: 2 mm, and length: 50 mm). The graphite rods were used as electrodes on both sides of the quartz tube, and the graphite rods were attached to conductive copper foil to prevent the heated powder from escaping through the space between the graphite block and the quartz tube. Then, the quartz tube was loaded into the reaction stage and connected to the FJH apparatus. A capacitor bank (capacitance of 60 mF) was used to provide a direct discharge current with maximum voltages up to 400 V, which can heat the sample to temperatures up to 3000 °C in a few seconds and effectively convert an amorphous carbon to graphitic carbon [36]. Then a pulse of 300 V was applied to the mixed powder sample under a mild vacuum (~10 mmHg) for ~5 s. After the FJH reaction, the apparatus was cooled naturally after 5 min to room temperature. The sample was removed from the quartz tube, ground with a mortar and pestle, and then washed repeatedly with HCL acid and deionized water. Finally, after drying for 24 h under a vacuum at 60 °C, the resultant graphitized coal material was denoted as FHC.

2.2. Materials characterization

An X-ray diffractometer (XRD) with a CuKα radiation source (λ = 1.5418 Å) was used to analyze the phase and crystalline structures of coal samples. The interlayer distance d_{002} was calculated using Bragg's equation [39]. Raman spectra were recorded using Raman spectroscopy (Horiba Jobin Yvon, LabRAM HR800) to study the disordered and graphite structure in the samples. Transmission electron microscopy and high-resolution translation electron microscopy (TEM, HR-TEM JEOL, JEM-2100 with Bruker super-X EDX model) were used to characterize the nanostructures of the samples, and analytical scanning electron microscopy (SEM, JEOL, JSM-6480A) was used to examine the surface morphology of coal samples. The Brunauer–Emmett–Teller surface area was performed using Micro TriStar II Plus 2.02.

2.3. Electrochemical measurements

The electrode slurries were made by mixing graphitized coal materials (HTC or FHC as active materials) (80 wt%) with the binder of polyvinylidene fluoride (PVDF) (10 wt%) and a conducting additive of carbon black (Super P) (10 wt%) under magnetic stirring using the solvent of *N*-methyl-2-pyrrolidone (NMP) in order to make a homogeneous slurry. After being stirred for 4 h, the obtained slurries were coated on a clean copper foil with a 75 µm thickness and vacuum-dried at 65 °C for 24 h. The obtained foils were roll-pressed and punched into circular discs of 12 mm in diameter. Every disc was weighed with a deduction of copper foil weight, and the specific capacity of the electrode was calculated according to the active material's total weight. The electrochemical performance of the samples was measured by coin cells of type CR2023, which were fabricated in the glove box filled with argon gas, and maintained with oxygen and moisture levels below 0.1 ppm. For LIBs, the counter electrode was made out of pure lithium foil, a Celgard 2400 polypropylene membrane was used as a separator, and 1.0 M LiPF6 in ethylene carbonate/dimethyl carbonate (EC/DEC) (1: 1 by volume) as the electrolyte solution. For PIBs, the counter electrode was made out of pure potassium foil, with the separator of (Whatman) GF/C glassy fiber, and using 0.8 M KPF6 in the mixture of ethylene carbonate/diethyl carbonate (EC/DEC) (1: 1 by volume) as the electrolyte solution.

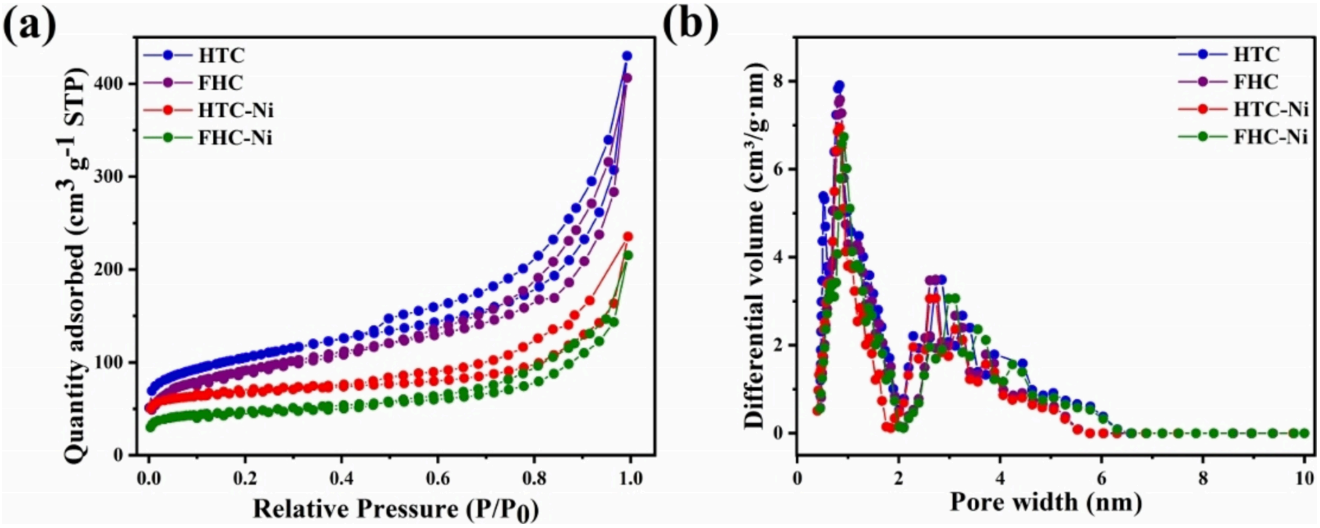

Fig. 2. (a) N_2 adsorption/desorption isotherms and (b) pore size distributions curves of the prepared samples.

To ensure the electrolyte was sufficiently permeated into the electrodes, all manufactured cells were aged for 16 h before being measured. The NEWARE battery test system (CT-4008 model) was used to perform the galvanostatic charge and discharge analyses over the voltage ranging from 0.01 to 3.00 V at room temperature. The electrochemical impedance spectroscopy (EIS) and cyclic voltammetry (CV) investigations were carried out using the IVIUMnSTAT multichannel electrochemical analyzer, with the (EIS) at a frequency ranging from 100 kHz to 10 mkHz and (CV) scan rate at 0.1 mV s^{-1}.

3. Results and discussion:

XRD and Raman spectroscopy measurements were carried out to investigate the structural changes and crystallinity of the coal samples. The XRD analysis results of the HTC and FHC samples before and after acid treatment, as well as the RC sample, are shown in Fig. 1a. After catalytic graphitization with the Ni catalyst, XRD patterns showed obvious differences between the RC pattern and other patterns, which indicate structural changes in the raw coal as a result of catalytic graphitization with the Ni catalyst. For the samples before acid treatment, the HTC-Ni pattern observed peaks at 44.3°, 51.6°, and 76.1° were indexed as the (1 1 1), (2 0 0), and (2 2 0) planes of the cubic nickel (PDF no. 65–0380), respectively, as well as a diffraction peak, which appears at 26.2° corresponding to the graphite plane (0 0 2) (PDF no. 89–8487). In contrast, the FHC-Ni pattern displayed peaks at 26.3° corresponding to the (0 0 6) hexagonal carbon (PDF no. 26–1076) and at 45°, representing the (1 0 1) plane of the cubic nickel (PDF no. 89–7129).

In addition, after removing Ni by the subsequent acid washing process, no Ni reflection peaks were observed in the patterns of HTC and FHC. For both samples, XRD patterns exhibit sharp and strong diffraction peaks around 26.2° and weak diffraction peaks appearing at 44.3°, which corresponded to the (0 0 2) and (1 0 1) reflections of graphitic carbon (PDF no. 41–1487). Compared with the RC pattern, these results showed that the raw coal structure had been transformed from amorphous to crystalline after applying catalytic graphitization using the FJH and traditional heating methods, which can contribute to their electrochemical behavior and provide Li^+ and K^+ additional storage sites. The calculated d-spacing (d_{002}) values were about 0.34 nm for HTC and FHC, which is close to the graphite d-spacing (0.335 nm), indicating both samples have good crystallinity.

The Raman spectra further supported the XRD results. Fig. 1b compares the spectrum of RC samples with the spectrums of HTC and FHC samples before and after acid treatment. It can be seen that all samples except RC have three distinctive peaks of D, G, and 2D bands, located at roughly 1350, 1585, and 2900 cm^{-1}. Generally, the D-band represents disordered and defective carbon. In contrast, the G-band corresponds to the in-place vibration motion of the sp2-bond of carbon atoms, indicating the information of graphitic carbon [40]. Moreover, the 2D-band represents the presence of highly ordered graphitic layers in the carbon matrix [28]. Additionally, the peak intensity ratio (ID/IG) also characterizes the carbon material's defect, disorder, and graphitization degrees [41]. Narrower G-band widths and lower ID/IG values usually indicate a higher degree of graphitization with a more ordered and perfect graphite structure [42,43]. There is a slight decrease in the values of (ID/IG) for the HTC and FHC samples after acid treatment, demonstrating an increase in the graphitization degree after the removal of Ni. Furthermore, the ID/IG values of HTC and FHC are about 0.73 and 0.75, respectively. These lower values demonstrate that the obtained samples contain a high degree of graphitization. These results are in agreement with those obtained from the XRD analysis.

Table 1
The porous structure parameters of the prepared samples.

Parameters	HTC-Ni	HTC	FHC-Ni	FHC
Specific surface area (m^2/g)	281	372	268	357
Total pore volume (m^3/g)	0.42	0.52	0.41	0.47
Micropore volume (m^3/g)	0.31	0.36	0.32	0.33
Mesopore volume (m^3/g)	0.11	0.16	0.09	0.14
Average pore diameter* (nm)	2.01	2.24	1.94	2.13

* IUPAC classifications: micropore (<2 nm), mesopore (2 to 50 nm), macropore (>50 nm).

The BET measurements were used to study the prepared samples' specific surface area and pore size distribution. The N_2 adsorption/desorption isotherm curves and pore size distribution of the samples are shown in Fig. 2, and the porous structure parameters are listed in Table 1. Obviously, all samples in Fig. 2a display the IV isotherm adsorption/desorption curves according to the IUPAC classification, presenting the existence of micropores and mesopores. Fig. 2b shows the pore size distribution of the samples; it is clear that all samples mainly contained micropores (distributed between 0.4 and 2.0 nm) and a certain amount of mesopores (ranged from 2.0 to 6.3 nm). Furthermore, as shown in Table 1, the prepared samples' acid treatment increased the surface area from 281 to 372 m^2/g for HTC and from 268 to 357 m^2/g for FHC. Similarly, the total pore volume of HTC increased from 0.42 to 0.52 m^3/g and from 0.41 to 0.47 m^3/g for FHC. These results indicate that the removal of the catalyst produces more porous carbon, which is beneficial to improving the electrochemical performance of the

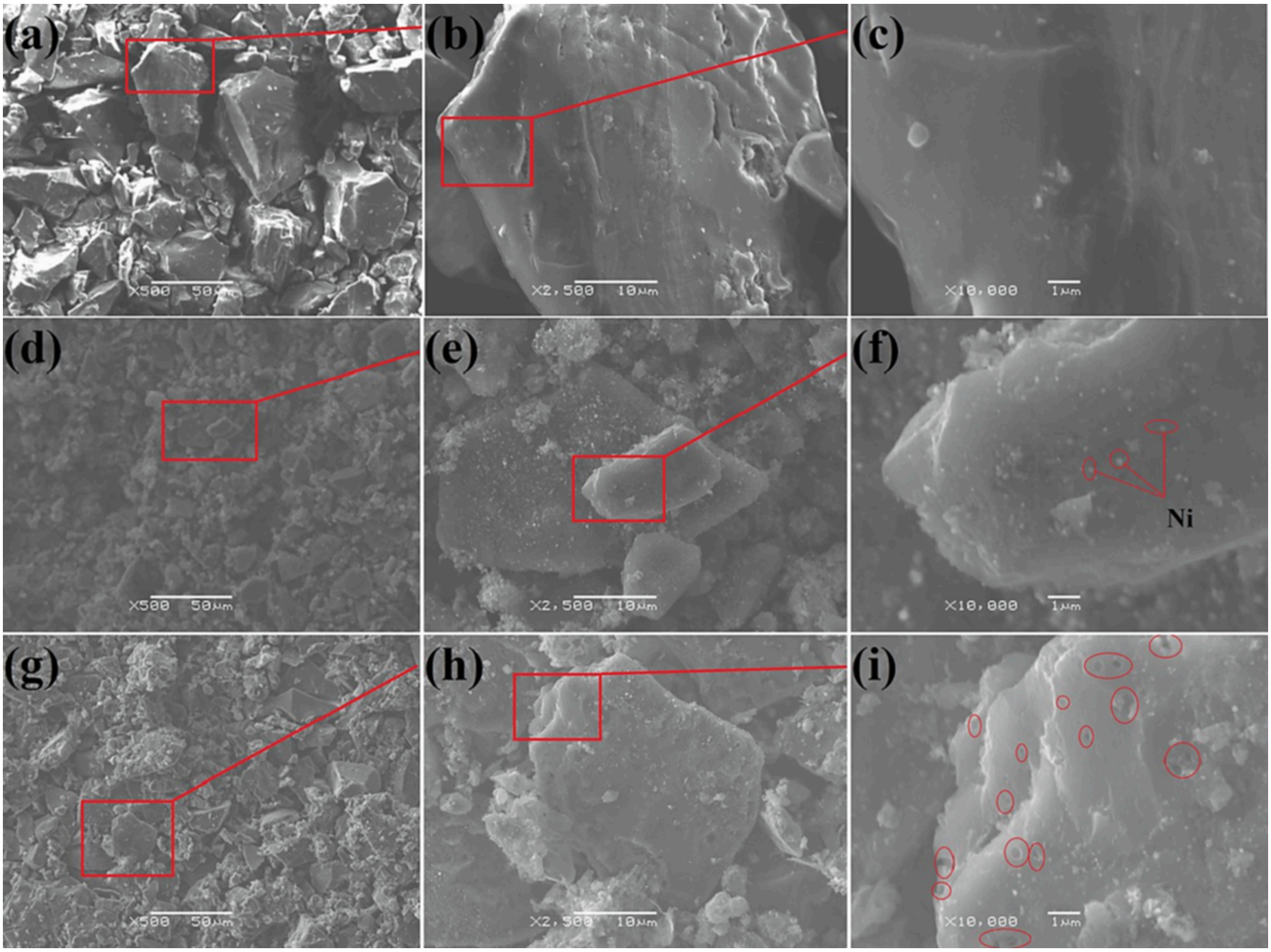

Fig. 3. SEM images of RC (a–c), HTC-Ni (d–f), and HTC (g–i).

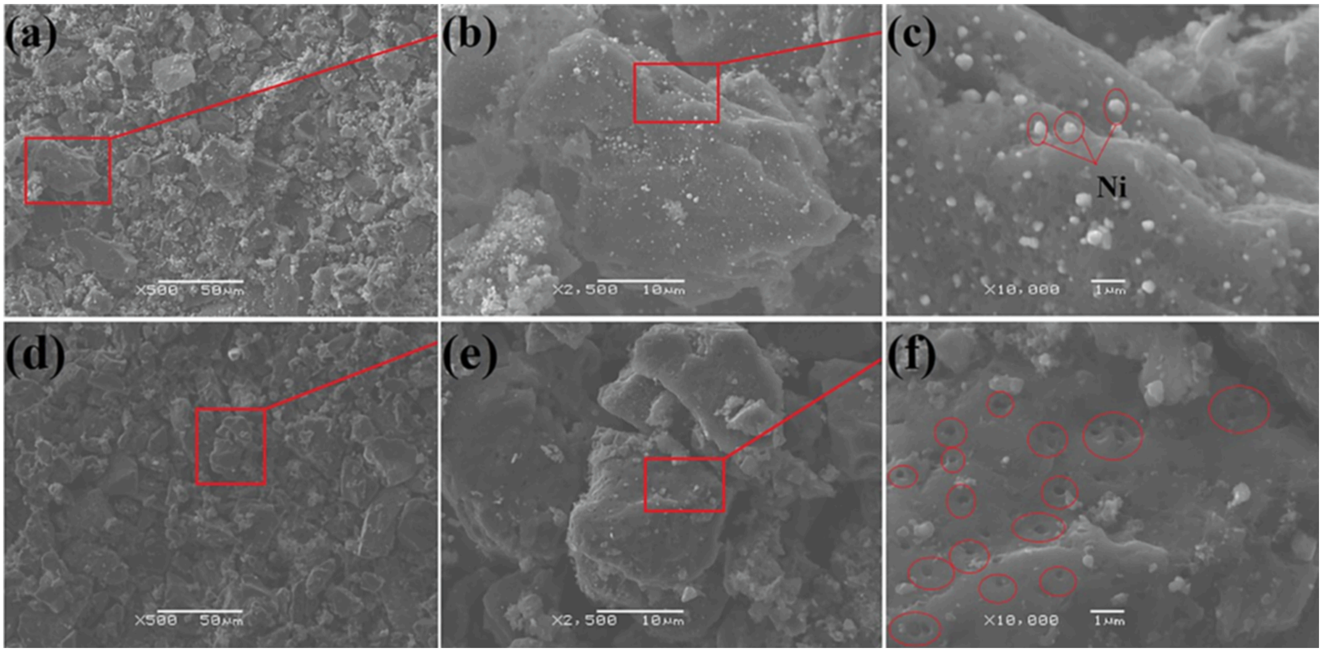

Fig. 4. SEM images of FHC-Ni (a–c), FHC (d–f).

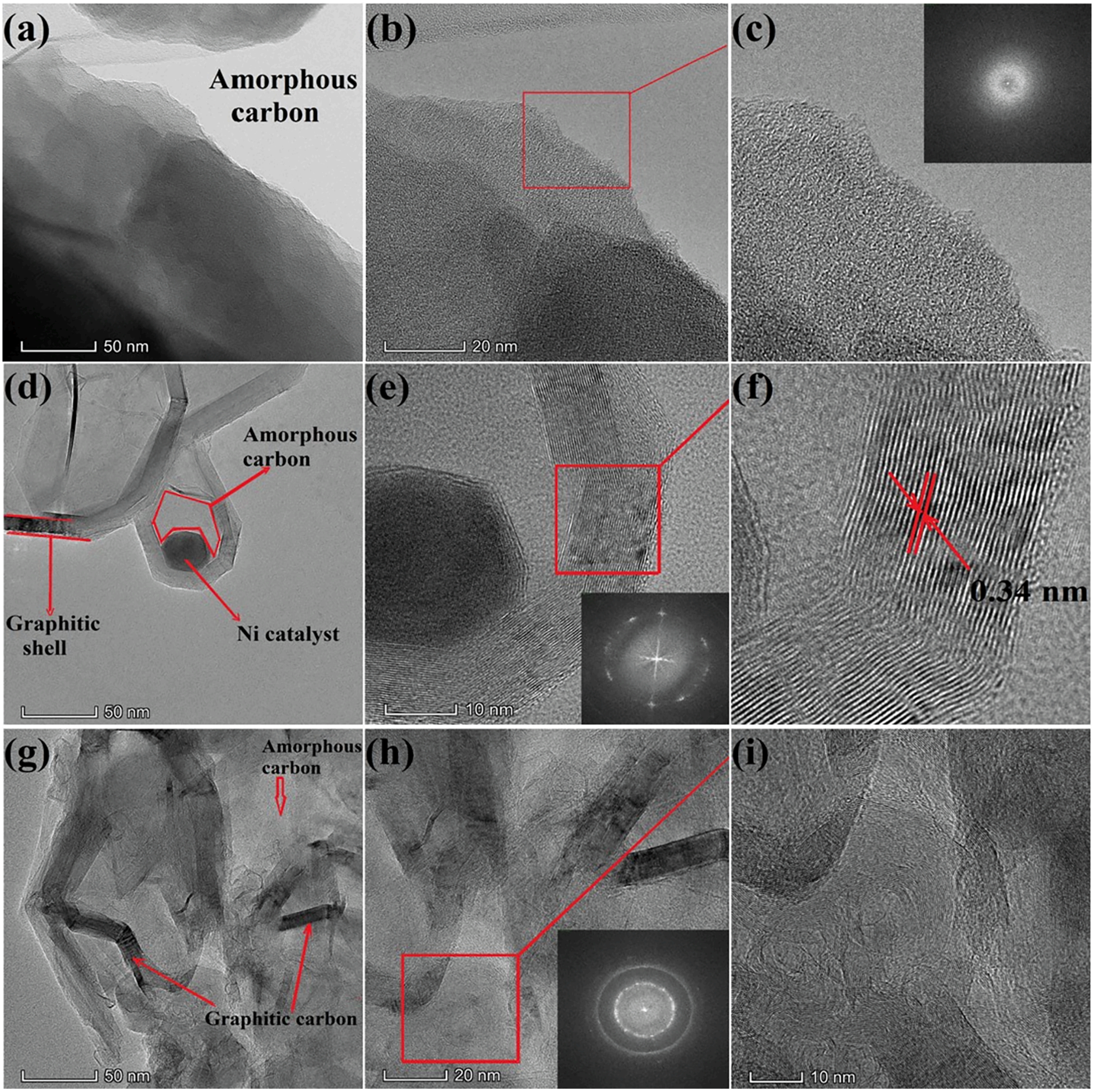

Fig. 5. TEM and HR-TEM images of RC (a–c), HTC-Ni (d–f), and HTC (g–i).

material. Since the micropores provide the surface area for charge storage, while the mesopores provide the channel for ions transport [27].

Scanning electron microscopy (SEM) tests were performed to study further the microstructure changes of the HTC and FHC samples prepared by the catalytic graphitization process. The images at various magnifications are displayed in Figs. 3 and 4. The RC sample structure in Fig. 3a is relatively dense, and the material is distributed in irregular blocks. The surface in Fig. 3b is smooth and relatively flat, and there are no pores or holes as shown at low magnification in Fig. 3c. In Fig. 3d and Fig. 4a, the SEM images of the HTC and FHC samples before acid treatment are shown; both samples have irregular shapes, attached by small particles, as seen in Fig. 3e and Fig. 4b. There is a homogeneous distribution of spherical Ni-catalyst particles (particles noticeable in red circles) throughout the surface, as seen in Fig. 3f and Fig. 4c. In contrast, after two-step acid treatment of HCL and deionized water of the HTC and FHC samples, the SEM images in Fig. 3g and Fig. 4d show that both samples have an uneven granular morphology. As shown in Fig. 3h and Fig. 4e, their surfaces were no longer smooth and not flat as in the RC sample. At low magnification, as shown in Fig. 3i and Fig. 4f, these samples have a relatively rough surface, and there are rich pores of different sizes (surrounded by red circles), which facilitate the transport of electrolyte ions [27]. These results demonstrate that the catalytic graphitization process can enhance pore development using both methods.

To further investigate the structural change of coal samples and also describe the formation of graphitic nanostructures in the obtained samples, transmission electron microscopy (TEM) and high-resolution translation electron microscopy (HR-TEM) coupled with fast Fourier transform (FFT) were performed. Figs. 5 and 6 show the TEM results,

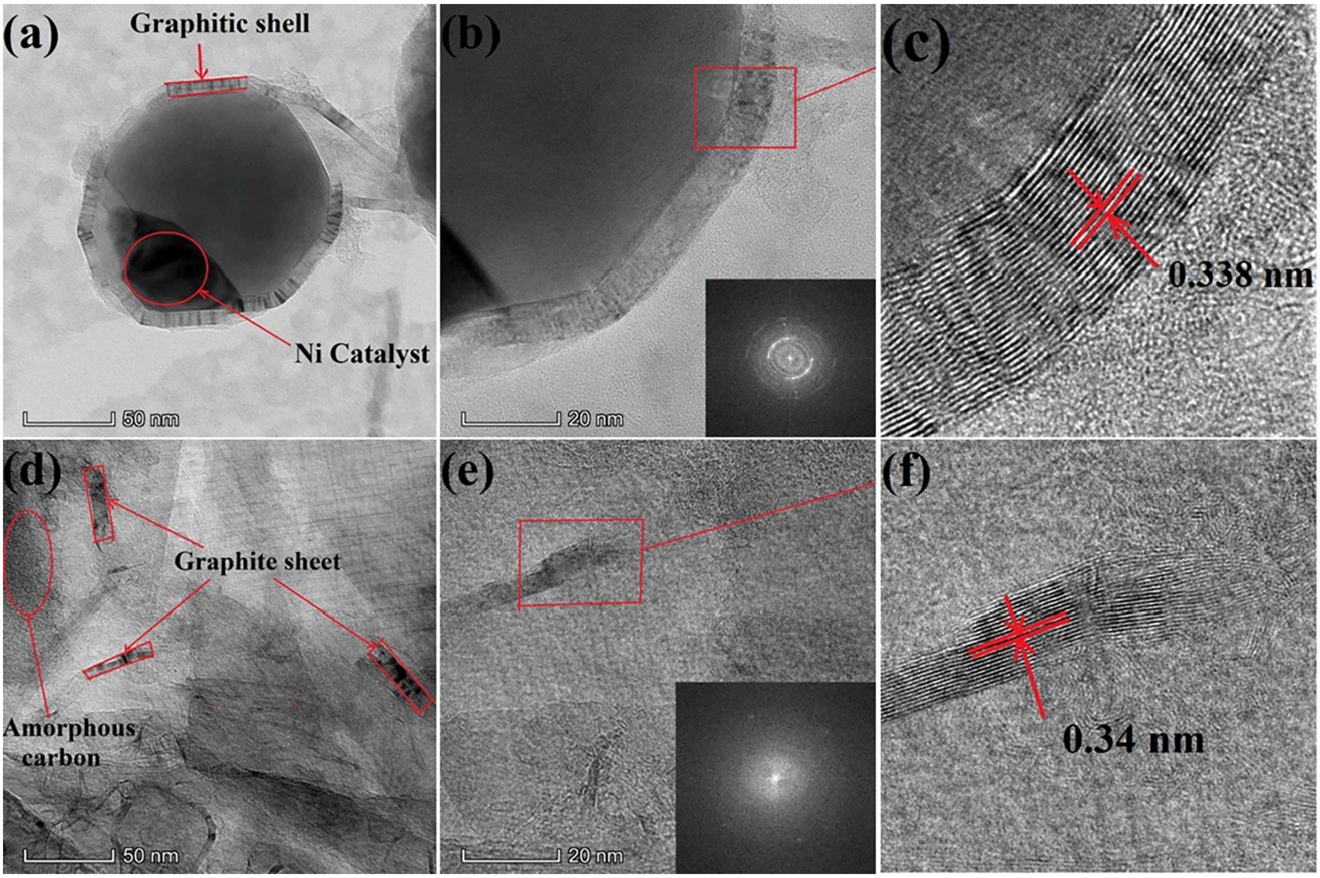

Fig. 6. TEM and HR-TEM images of FHC-Ni (a–c), and FHC (d–f).

which are agreeable with XRD, Raman, and SEM analysis. Before catalytic graphitization, the RC sample was amorphous, as shown in Fig. 5a, and there are no graphitic domains in the HR-TEM image in Fig. 5b. The FFT image shows a hollow circle (upper inset), as shown in Fig. 5c, which further confirms the amorphous structure of the RC. TEM and HR-TEM were also performed to study the structure of the HTC sample after catalytic graphitization and before acid treatment. As shown in Fig. 5d, HTC-Ni consists of graphitic carbon, which is mainly produced by chemical interaction between the amorphous carbon and the Ni catalyst nanoparticles at high temperatures. With the diffusion of Ni particles throughout the amorphous carbon matrix and an increase in the temperature, only the carbon in contact with the Ni nanoparticles was converted into a precipitate graphitic nanostructure. The rest of the material remains as amorphous carbon. In addition, the diffusion of nickel particles ended when they met the stiff graphitic layers. As a result, the HTC-Ni sample contains amorphous carbon mixed with multilayered graphitic carbon around the catalyst. This is seen in the FFT (lower inset) and HR-TEM images in Fig. 5e. Fig. 5f clearly shows highly crystallized carbon layers separated by an interlayer distance of 0.34 nm (from the XRD result). After acid washing and subsequent deionized water washing of the HTC-Ni sample, the catalyst was removed. The TEM image of the HTC sample in Fig. 5g shows the retention and high crystallinity of graphitic nanostructures mixed with a small amount of amorphous carbon. As in the HR-TEM and FFT (in the inset) images in Fig. 5h, which also show high crystallinity nanostructures. Moreover, as shown in Fig. 5i, the low-magnification HR-TEM image indicates the highly ordered graphite crystalline structure mixed with a small amount of amorphous carbon.

After catalytic graphitization using flash Joule heating (FJH), the amorphous structure of raw coal was transformed into a crystalline structure. TEM images of the FHC-Ni and FHC samples in Fig. 6 and by comparison with the images of RC samples in Fig. 5a − c confirmed this transformation. As illustrated in Fig. 6a, the TEM image of the FHC-Ni sample shows the graphitized carbons of a typical circle-like nanostructure. This nanostructure consists of a dark area (Ni particles-rich side) embedded in a large (carbon-rich side) area. The graphitic carbon is produced during Joule heating by moving catalyst nanoparticles through the amorphous carbon areas, precipitating as graphitic ordered layers. Consequently, the graphitic shell's form shows a ring-like structure of highly crystallized carbon with different curvatures. The HR-TEM image in Fig. 6b shows the formation of a ribbon-like graphitic nanostructure of the FHC-Ni sample. The FFT image (right lower inset) confirmed that graphitic nanostructures or crystalline ordering were formed in this sample. Fig. 6c shows clearly highly crystallized carbon layers, separated by an interlayer distance of 0.338 nm (from the XRD result). After acid washing and subsequent deionized water washing, Ni particles were almost completely dissolved and removed from the sample. So, no metal nanoparticles were observed in the TEM image of the FHC sample in Fig. 6d − f. As shown in Fig. 6d, the TEM image clearly shows that the FHC sample contains widespread-layered graphite sheets mixed with a small amount of amorphous carbon. The HR-TEM in Fig. 6e also showed a highly ordered graphite crystalline structure. The FFT image (right–bottom inset) showed multiple sets of dots with sixfold symmetry, indicating the more clearly crystalline ordering of the FHC sample. The interlayer distance of graphitic material has changed slightly, as shown in Fig. 6f; after acid washing, it was about 0.34 nm (based on the XRD result). These observations provide another proof to confirm the transformation of the raw coal structure from amorphous into crystalline when the raw coal was prepared with the metal catalyst and heated by both heating methods.

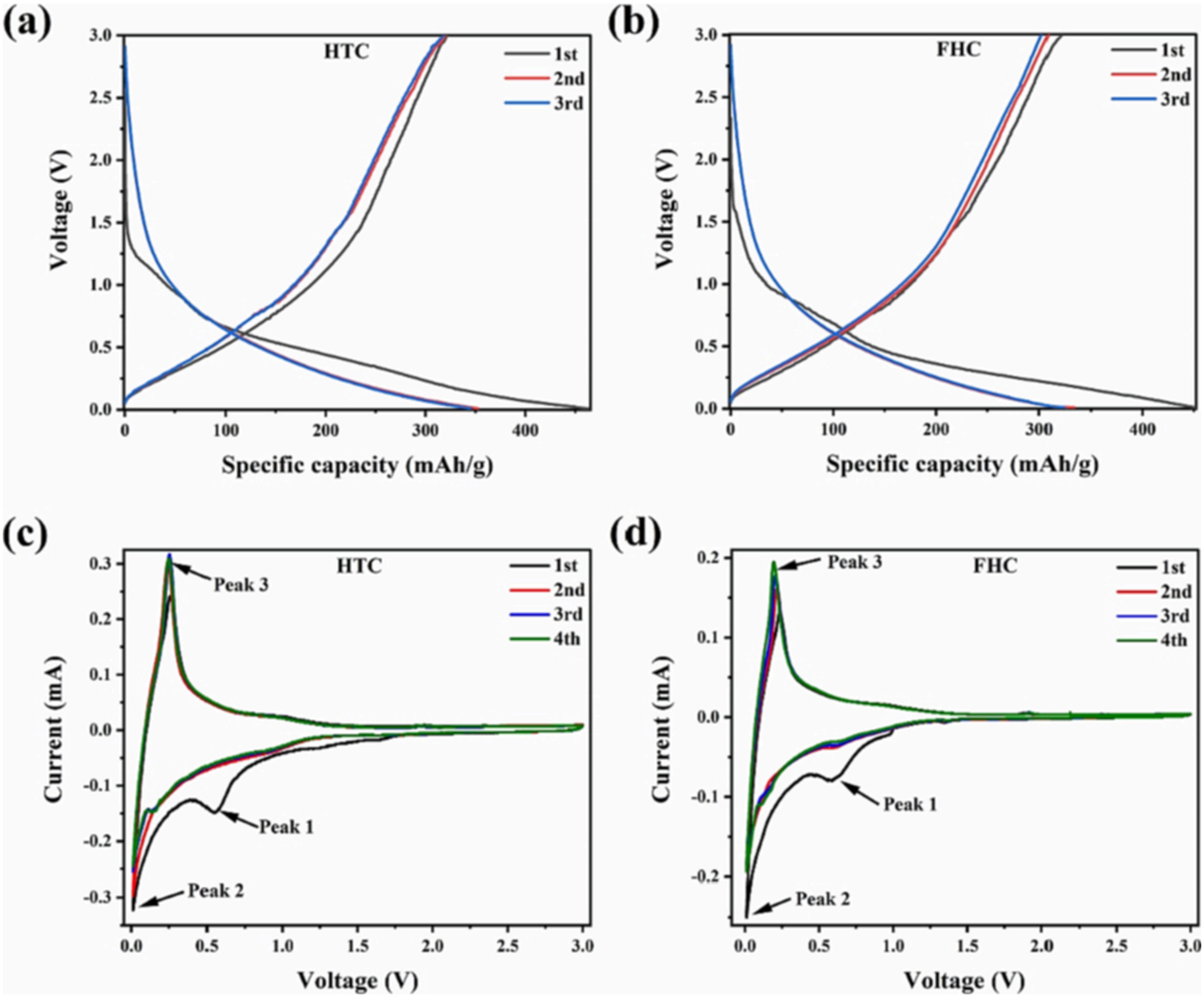

Fig. 7. Electrochemical performance of HTC and FHC tested against Lithium: charge/discharge curves (a) and (b); cyclic voltammetry (c) and (d).

4. Electrochemical performance measurements

4.1. Electrochemical performance as anodes of LIBs.

To evaluate the lithium storage property of graphitized coal materials and compare the performance of HTC and FHC samples as anode materials in LIBs, half-cell batteries were assembled. Galvanostatic charge and discharge profiles of HTC and FHC electrodes were obtained from 0.01 to 3 V versus Li/Li^+ at a 0.1C current density rate, as displayed in Fig. 7a and b. The initial charge (lithiation) and discharge (delithiation) capacities of the HTC are 322.5 and 463 $mAh\cdot g^{-1}$, as shown in Fig. 7a, and 321.3 and 450.6 $mAh\cdot g^{-1}$ for the FHC, as indicated in Fig. 7b. The initial coulombic efficiency (ICE) was about 69.6 % and 71.3 % for HTC and FHC, respectively. These poor coulombic efficiency values can be mainly attributed to forming the solid electrolyte interface (SEI) on the surface of electrodes and the irreversible part of lithium storage [11]. Such a loss of capacity in the first cycle is common amongst carbon materials. In the subsequent cycles, this phenomenon disappeared, and the coulombic efficiencies increased gradually for both electrodes. In the second and third cycles, the coulombic efficiency reached 90.9 % and 92.3 % for the HTC and 92.6 % and 93.4 % for the FHC, respectively, demonstrating stable electrochemical performance.

Comparing the initial charge capacities of the carbon materials prepared in this work with different carbon materials reported in the literature is shown in Table 2. Carbons included in the comparison are TNO nanoparticles [44], tetrakis coumarin [45], anthracite-based graphite [46], Mg-doped LZT/C [47], regenerated graphite [48], graphitized stacked-cup carbon nanofibers [49], graphitized boron-

Table 2
The electrochemical performance comparison of HTC and FHC with a variety of carbonaceous materials as anodes for the materials of LIBs.

Material name	Charge capacity ($mAh\cdot g^{-1}$)	Ref
TNO	201 at (0.1C)	[44]
TKC	238 at (0.05C)	[45]
AF/2800	250 at (0.1C)	[46]
LZMT/C	260 at (0.2C)	[47]
R-Gr	280 at (0.05C)	[48]
PR19–2800	295 at (0.1C)	[49]
9.0PB24	310 at (0.1C)	[50]
B/CIQ5/2600	310 at (0.1C)	[51]
BCNF	310.3 at (0.1C)	[24]
PET Coke	320 at (0.1C)	[8]
HTC	322.5 at (0.1C)	This work
FHC	321.3 at (0.1C)	This work
BCG-2800	324.6 at (0.1C)	[52]
BCG-2600	325 at (0.1C)	[52]

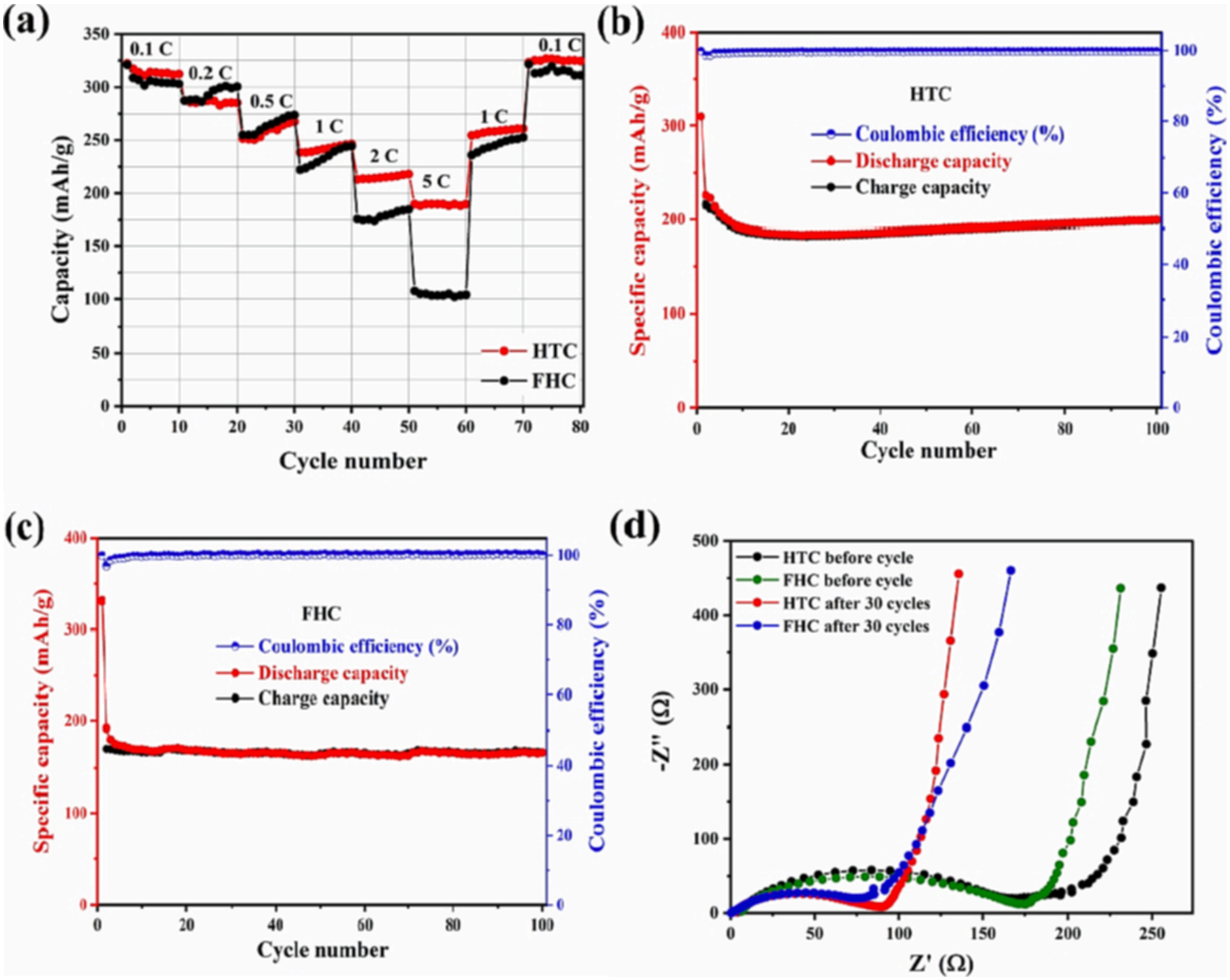

Fig. 8. (a) Rate performance of HTC and FHC. (b) and (c) cycling performance of HTC and FHC at a current rate of 2C. (d) EIS curves of HTC and FHC before and after 30 cycles.

doped carbon foams [50], graphite materials prepared from coal combustion fly ashes [51], graphitized biogas-derived carbon nanofibers [24], carbons from petroleum coke [8] and synthetic graphite from bituminous coal [52]. Compared to most other carbon materials, it can be estimated that the overall performance of both HTC and FHC samples is better in terms of initial charge capacity and slightly lower than that of BCG-2800 and BCG-2600.

The cyclic voltammetry (CV) measurements for HTC and FHC were carried out at a scan rate of 0.1 mV s^{-1} in the voltage range from 0.01 V to 3.0 versus Li/Li^{+}. The first four CV profiles are shown in Fig. 7c and d. Similar CV profiles can be noted between HTC and FHC. The broad reduction peak (peak 1) in the initial cycle is located between 0.5 and 0.6 V. This is because of the forming of dense (SEI) layers on the electrode surface due to the electrolyte decomposition reaction [53]. It is worth noting that this peak disappeared in the subsequent cycles, which confirms that the carbon structure and SEI film formation have stabilized. The distinctive reduction peak can be shown at approximately 0.015 V at peak 2; this peak is attributed to the intercalation of lithium ions into the graphitic carbon structure of anode materials. In addition, during charging, a sharp and strong oxidation peak is observed between 0.2 V and 0.25 V at peak 3, which is related to the deintercalation of lithium ions from the graphitic carbon structure. Above all, after the initial cycle, the CV curves almost overlapped each other, indicating excellent electrochemical reversibility of the HTC and FHC anode materials.

For more comparison between the differences in the electrochemical behavior of HTC and FHC, Fig. 8a displays the rate performance of six current rates from 0.1C to 5C for 10 cycles each and their corresponding charge/discharge profiles. At a low current rate of 0.1C, the HTC electrode's initial charging capacity was 322.2 $mAh{\cdot}g^{-1}$ and maintained about 314.3 $mAh{\cdot}g^{-1}$ during the subsequent cycles. Following the gradual increase in current rates, the average charging capacities of 285, 258.2, 242, 215, and 189.2 $mAh{\cdot}g^{-1}$ were obtained at current densities of 0.2C, 0.5C, 1C, 2C, and 5C, respectively. In contrast, the FHC presents an initial charging capacity of 321.1 $mAh{\cdot}g^{-1}$ (maintains about 306.4 $mAh{\cdot}g^{-1}$ during the subsequent cycles) at a current rate of 0.1C. The average charging capacities of 293.8, 263.7, 233.8, 178.8, and 104.3 $mAh{\cdot}g^{-1}$ were obtained at current densities of 0.2C, 0.5C, 1C, 2C, and 5C, respectively. The higher rate capability and better reversibility at a current rate of 0.1C can be seen from the HTC electrode when compared to FHC. This indicates that it has a more favorable rate capability. Moreover, after 60 cycles of charging and discharging with various current densities, once the current rate suddenly reverted to 1C and 0.1C, the HTC electrode recovered the average charge capacities of 258.3 and 325.2 $mAh{\cdot}g^{-1}$, respectively. Similarly, the FHC electrode recovered charge capacities of 245.5 and 315 $mAh{\cdot}g^{-1}$. These results indicate that both samples have outstanding cycling stability and rate performance as anode materials for LIBs.

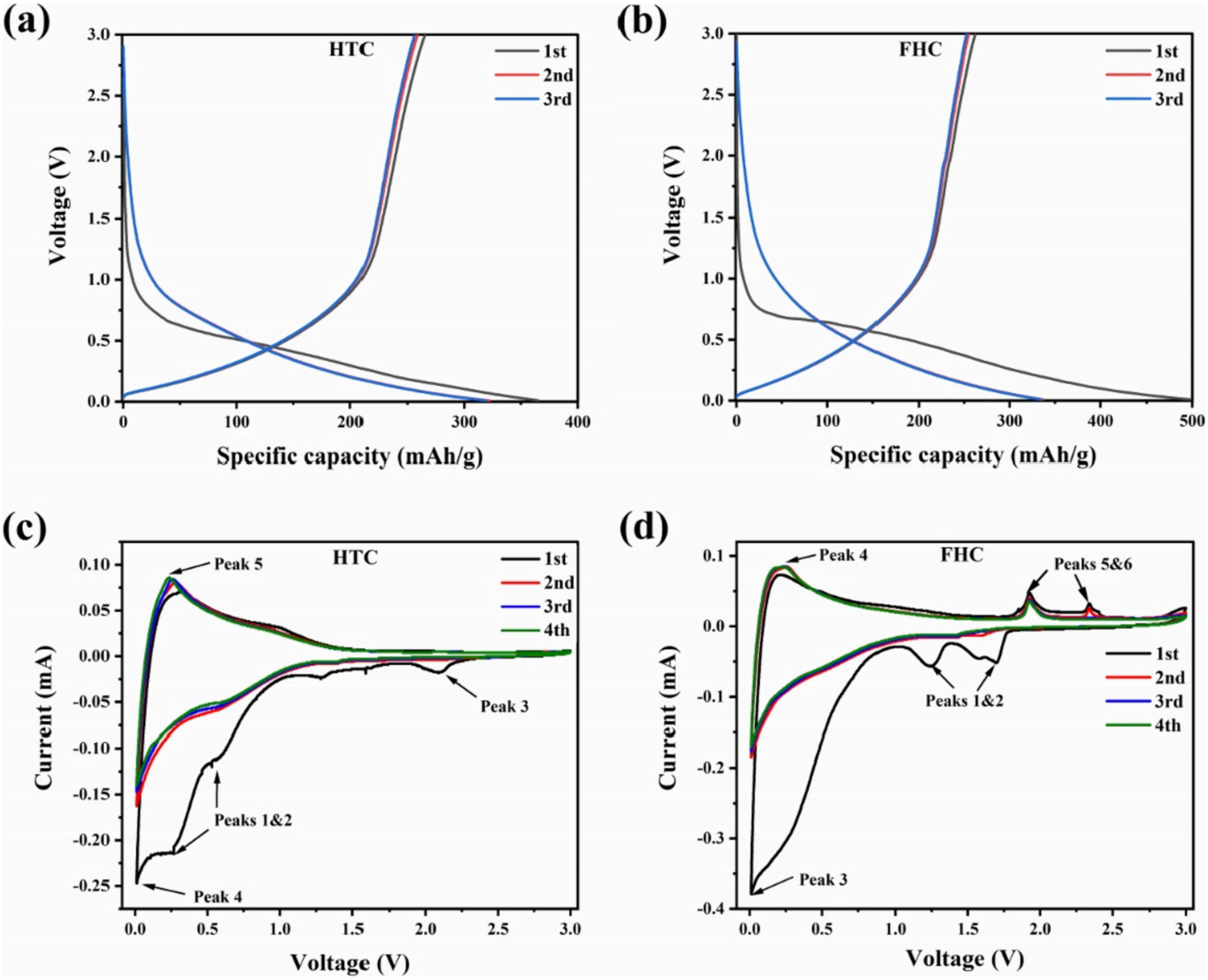

Fig. 9. Electrochemical performance of HTC and FHC tested against Potassium: charge/discharge curves (a,b) and cyclic voltammetry (c,d).

Additionally, Fig. 8b and c display the cycling behavior and coulombic efficiency of HTC and FHC electrodes after 100 cycles at a 2C current rate. As we can see, during the initial charge cycle, the HTC exhibited a capacity of 215.8 mAh·g^{-1}, and it still had a capacity of 199.2 mAh·g^{-1} after 100 cycles with a roughly 99 % capacity retention rate. Besides, FHC exhibits an initial charge capacity of 179.6 mAh·g^{-1} and after 100 cycles 166.1 mAh·g^{-1}, with coulombic efficiency of nearly 99 %. These results indicate the excellent cycling performance and electrochemical stability of the obtained samples as anode materials for LIBs. The electrochemical impedance spectroscopy (EIS) experiment was carried out to investigate the kinetics of electrodes and to explain the reasons for the excellent performance of the prepared samples as anode materials for LIBs. The tests were performed before and after 30 charge/discharge cycles and recorded at a frequency ranging between 100 kHz and 10 mkHz. The Nyquist plots of HTC and FHC electrodes shown in Fig. 8d are similar in shape. The Nyquist plots consist of a high-frequency semicircle range corresponding to charge transfer resistance (R_{ct}) at the interface between electrode and electrolyte and a low-frequency inclined line corresponding to the Warburg impedance of the Li-ions diffusion process through the electrode [53]. These results are consistent with the galvanostatic charge and discharge and C.V tests. Moreover, the HTC electrode has a slightly smaller semicircle diameter than that of FHC, indicating a lower (R_{ct}) and higher electrical conductivity. Furthermore, after 30 charge/discharge cycles, the Nyquist plots of HTC and FHC show very little difference between before and after cycling, indicating that the prepared samples have good electrochemical stability as LIBs anode materials.

Table 3
Comparison of electrochemical performance between HTC and FHC with different carbon materials as anodes of materials of PIBs.

Material name	Charge capacity (mAh·g^{-1})	Ref
TC1100	195 at (0.1C)	[54]
TC1600	200 at (0.1C)	[54]
SnS@C	205 at (0.1C)	[55]
NSO-HCN	238 at (0.05C)	[56]
SC	246 at (0.1C)	[16]
Nano-CaCO3	259 at (0.05C)	[57]
HCS-SC	261 at (0.1C)	[16]
S-3DHPC-4	~ 248 at (0.05C)	[58]
EG	~ 220 at (0.05C)	[59]
HTC	265.4 at (0.1C)	This work
FHC	262.2 at (0.1C)	This work
B1-A-900	~ 270 at (0.05C)	[23]
PGC	~ 285 at (0.05C)	[33]

4.2. *Electrochemical performance as anodes of PIBs.*

The K-ion storage properties of HTC and FHC samples were tested

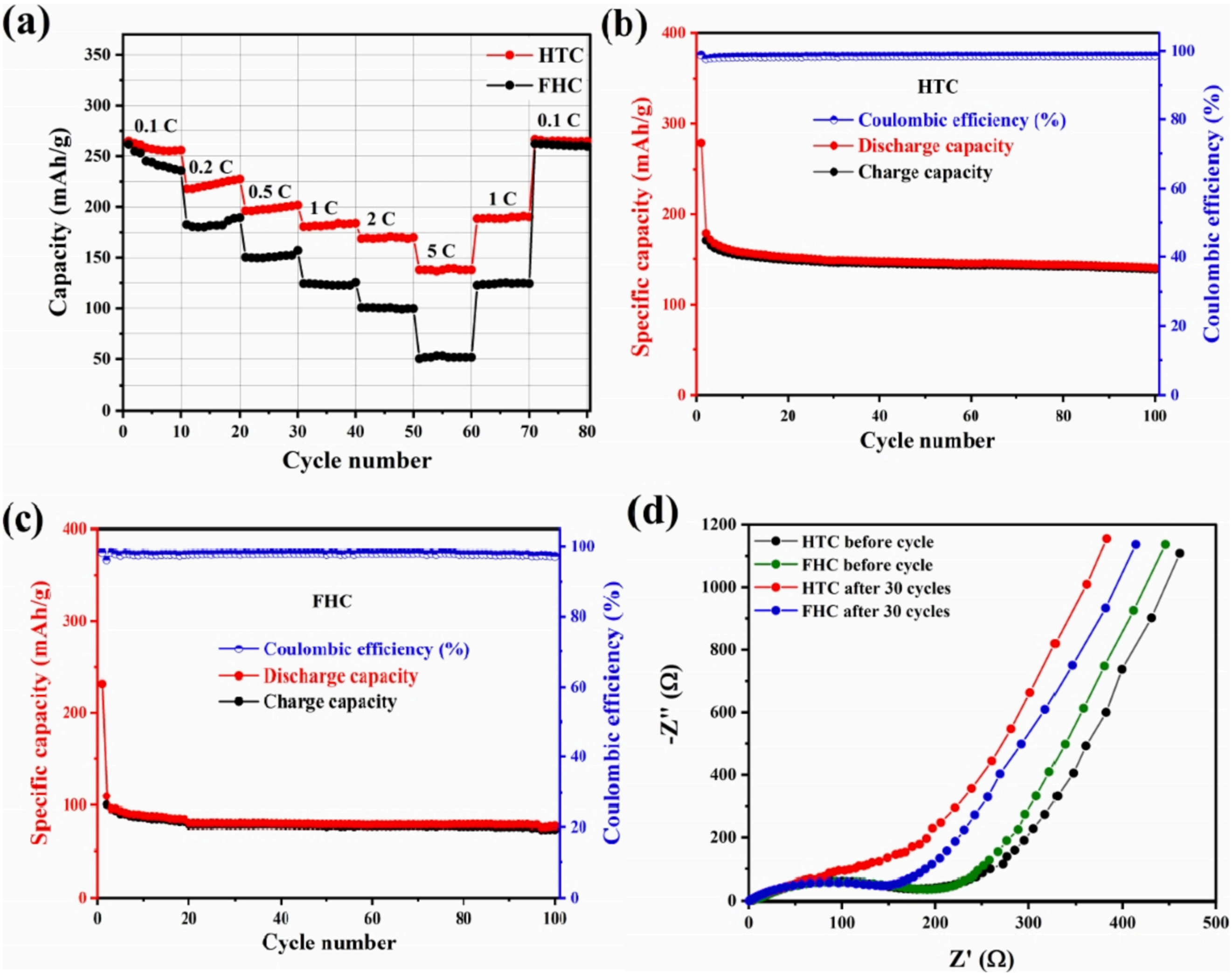

Fig. 10. (a) Rate performance of HTC and FHC.(b,c) cycling performance of HTC and FHC at a current rate of 2C. (d) EIS curves of HTC and FHC before and after 30 cycles.

using potassium metal as a reference electrode/counter. Fig. 9a and b display the charge (potassiation) /discharge (depotassiation) profiles of HTC and FHC as the anodes materials for PIBs under a current density rate of 0.1C and voltage range between 0.01 and 3.0 V versus K/K^+. The electrodes delivered initial charging and discharging capacities of 265.4 and 365.2 $mAh{\cdot}g^{-1}$ for the HTC and 262.2 and 498.1 $mAh{\cdot}g^{-1}$ for the FHC, with an ICE of 72.6 % for HTC and 52.6 % for FHC. The low ICE of both electrodes is certainly associated with forming the layer of (SEI) on the electrode surface, which is expected as in LIBs. The K-ion storage performance (initial charge capacities) of the HTC and FHC samples was also compared with different carbon materials, shown in Table 3. Carbons included for comparison are hard-carbon derived Waste-Tire Rubber [54], carbon-supported SnS [55], N/S/O-tridoped hard carbon [56], hard-soft composite carbon [16], hierarchically porous carbon prepared from the nano-CaCO3 template and sucrose [57], coal-derived S heteroatoms [58], expanded graphite [59], coal-based carbon [23] and nanoporous coal [33]. From Table 3, it can be evaluated that the HTC and FHC electrodes have better initial charge capacities than most of the other materials.

Fig. 9c and d exhibit the CV profiles of HTC and FHC electrodes which were measured over a voltage range between 0.01 and 3.0 V versus K/K^+, with a 0.1 mVs^{-1} scan rate for the first four cycles. Irreversible peaks were observed in the first cycle for both electrodes; for the HTC at 0.26 V, 0.59 V, and 2.1 V; for the FHC, they have observed at 1.25 V and 1.7 V. These peaks correspond to forming of SEI films due to the reaction of electrolyte decomposition as in the LIBs. Remarkably, in the subsequent cycles, these peaks almost disappeared for both electrodes, confirming that the SEI layer was formed only in the initial discharge cycle. The strong sharp cathodic peak at around 0.01 V was observed in the first four cycles for both electrodes because of the intercalation of the K-ions into the carbon pores. Besides, anodic peaks were located at ~ 0.25 V for HTC and ~ 0.22 V for FHC, which were associated with the K-ion extraction. Furthermore, the subsequent CV profiles overlapped well, indicating good cycling stability for both electrodes.

In addition, the rate performance was also measured at different current rates from 0.1C to 5C for HTC and FHC electrodes. As shown in Fig. 10a, significantly, the HTC electrode exhibits excellent rate performance compared to the FHC electrode. The HTC electrode presents average charge capacities of 258.1, 222.2, 198.4, 182.1, 169.3, and 138 $mAh{\cdot}g^{-1}$ at current rates of 0.1, 0.2C, 0.5C, 1C, 2C, and 5C, respectively. In contrast, when the current rate was increased gradually from 0.1 to 0.2C, 0.5C, 1C, 2C, and 5C, the corresponding average charge capacities of the FHC electrode were 254.1, 183.3, 151.4, 123.5, 100.1, and 51.8 $mAh{\cdot}g^{-1}$ respectively. Besides, once the current rates were switched back to 1C and 0.1C after 60 cycles, the initial charge capacity of both electrodes was increased, indicating excellent cycling stability and rate performance of the prepared samples as PIBs anode materials. The cycling performance and coulombic efficiency of the HTC and FHC electrodes over 100 cycles at a current density of 2C are shown in Fig. 10b and c. The HTC exhibits an initial charge capacity of 170.5 mAh·g^{-1}; after 100 cycles, the HTC has a capacity of 138.1 mAh·g^{-1}, with a retention ratio of nearly 98 %. In contrast, the FHC shows an initial charge capacity of 100.2 mAh·g^{-1} and maintains a capacity of 73.88 mAh·g^{-1} with a capacity retention of 97 % after 100 cycles. Overall, such high cycling performance and coulombic efficiency indicate the great potential of the obtained samples for energy storage applications again.

Moreover, the EIS technique for the HTC and FHC electrodes was performed before and after 30 cycles. As shown in Fig. 10 d, all the Nyquist plots are composed of one sloping line in the low-frequencies range and one depressed semi-circle in the high-medium frequencies range. The former is related to the solid diffusion impedance of the K-ions in the electrode and represents the Warburg impedance. The latter is associated with the charge transfer resistance (Rct) in the electrolyte/electrode interfaces [60]. In addition, after 30 cycles, the Nyquist plots of HTC and FHC show a slight difference between before and after cycling, demonstrating the good electrochemical performance of both electrodes.

5. Conclusion

In conclusion, the raw coal, an abundant and cheap source, was successfully converted from an amorphous structure into a crystalline structure by preliminary carbonization with catalytic activation followed by two different methods of graphitization; high-temperature treatment and flash Joule heating (FJH). The characterization results of XRD, Raman spectroscopy, BET, SEM, and TEM/HR-TEM showed structural changes and the formation of a crystalline structure. HTC and FHC anodes for LIBs delivered reversible capacities of 322.5 and 321.3 mAh·g^{-1}, respectively, at a 0.1C current density, with excellent rate capability and outstanding stable cycling performance. For PIBs, HTC and FHC anodes exhibit reversible capacities of 265.4 and 262.2 mAh·g^{-1}, respectively, at a 0.1C current density, with outstanding rate capability and stable cycling. The HTC anode demonstrated slightly better electrochemical performance than the FHC anode in both LIBs and PIBs. Despite these results, the conventional heating method of using a high-temperature furnace consumed a huge amount of energy and time. In contrast, the FJH heating process was easy, direct, and provided high temperatures within a very short time, as well as ultrafast cooling. This indicates that the FJH is much more efficient in terms of time and energy requirements than the current traditional heating method. Therefore, the catalytic synthesis method following FJH might become an economical and environmentally friendly alternative to producing anode materials for LIBs and PIBs, and the coal-based carbons might become a promising alternative to natural graphite.

CRediT authorship contribution statement

A.M.A. Mohamed: Writing – review & editing, Writing – original draft, Investigation, Data curation, Methodology, Conceptualization. **Shu Dong:** Formal analysis. **Maged Elhefnawey:** Writing – review & editing. **Guangsheng Dong:** Formal analysis. **Yinyi Gao:** Formal analysis. **Kai Zhu:** Supervision, Methodology, Writing – review & editing. **Dianxue Cao:** Funding acquisition, Supervision, Methodology, Writing – review & editing.

Declaration of Competing Interest

The authors declare that they have no known competing financial interests or personal relationships that could have appeared to influence the work reported in this paper.

Data availability

Data will be made available on request.

Acknowledgments

This work was supported by the Key Laboratory of Superlight Materials and Surface Technology (HEU10202213), Ministry of Education, High-level scientific research guidance project of Harbin Engineering University-bottleneck research plan (3072022QBZ1004).

References

[1] J. Ou, Y. Zhang, L. Chen, Q. Zhao, Y. Meng, Y. Guo, D. Xiao, Nitrogen-rich porous carbon derived from biomass as a high performance anode material for lithium ion batteries, J. Mater. Chem. A. 3 (2015) 6534–6541, https://doi.org/10.1039/c4ta06614f.

[2] J. Wang, P. Nie, B. Ding, S. Dong, X. Hao, H. Dou, X. Zhang, Biomass derived carbon for energy storage devices, J. Mater. Chem. A. 5 (2017) 2411–2428, https://doi.org/10.1039/c6ta08742f.

[3] Y. Dou, X. Liu, K. Yu, X. Wang, W. Liu, J. Liang, C. Liang, Biomass porous carbon derived from jute fiber as anode materials for lithium-ion batteries, Diam. Relat. Mater. 98 (2019) 107514, https://doi.org/10.1016/j.diamond.2019.107514.

[4] Y. Du, T. Gao, W. Ma, H. Li, Capacity fading of nanoporous carbon electrode derived from ZIF-8 during insertion-desertion of lithium ions, Chem. Phys. Lett. 712 (2018) 7–12, https://doi.org/10.1016/j.cplett.2018.09.051.

[5] C. Jo, S. An, Y. Kim, J. Shim, Nano-graphite functionalized mesocellular carbon foam with enhanced intra-penetrating electrical percolation networks for high performance electrochemical energy storage electrode materials, Phys. Chem. Chem. Phys. 14 (2012) 5695–5704, https://doi.org/10.1039/c2cp40657h.

[6] W. Zhang, X. Li, Y. Jin, G. Chen, Y. Li, S. Zeng, Nano-Co3O4 anchored helical carbon nanofibers as an anode material for Li-ion batteries, J. Electroanal. Chem. 922 (2022) 116730, https://doi.org/10.1016/j.jelechem.2022.116730.

[7] Q.L. Pan, J. Zhao, Y. Du, R. Liu, N. Li, B. Xing, S. Jiang, M. Pang, W. Qu, W. Liang, Z. Li, F. Cao, Coal-based kaolin derived porous silicon nanoparticles as anode materials for Li-ion batteries, Microporous Mesoporous Mater. 294 (2020) 109918, https://doi.org/10.1016/j.micromeso.2019.109918.

[8] O. Fromm, A. Heckmann, U.C. Rodehorst, J. Frerichs, D. Becker, M. Winter, T. Placke, Carbons from biomass precursors as anode materials for lithium ion batteries: New insights into carbonization and graphitization behavior and into their correlation to electrochemical performance, Carbon N. Y. 128 (2018) 147–163, https://doi.org/10.1016/j.carbon.2017.11.065.

[9] M. Jing, Z. Ding, H. Hou, Y. Zhang, G. Zou, S. Li, X. Ji, Alternating voltage induced electrochemical synthesis of three-dimensionalization copper oxide for lithium-ion battery application, Chem. Phys. Lett. 653 (2016) 30–34, https://doi.org/10.1016/j.cplett.2016.04.057.

[10] K. Wu, Y. Feng, J. Huang, C. Bai, M. He, Mo-doped 3D carbon@Sn as high performance anode material for lithium ion batteries, Chem. Phys. Lett. 756 (2020) 137832, https://doi.org/10.1016/j.cplett.2020.137832.

[11] X. Jin, Y. Li, J. Yao, K. Luo, J. Tan, Enhancing the Lithium Storage Performance of α-Ni(OH)2 with Zn2+ Doping, J. Electroanal. Chem. 922 (2022) 116747, https://doi.org/10.1016/j.jelechem.2022.116747.

[12] M. Wang, C. Jiang, S. Zhang, X. Song, Y. Tang, H.M. Cheng, Reversible calcium alloying enables a practical room-temperature rechargeable calcium-ion battery with a high discharge voltage, Nat. Chem. 10 (2018) 667–672, https://doi.org/10.1038/s41557-018-0045-4.

[13] Y. Shao, N.N. Rajput, J. Hu, M. Hu, T. Liu, Z. Wei, M. Gu, X. Deng, S. Xu, K.S. Han, J. Wang, Z. Nie, G. Li, K.R. Zavadil, J. Xiao, C. Wang, W.A. Henderson, J.G. Zhang, Y. Wang, K.T. Mueller, K. Persson, J. Liu, Nanocomposite polymer electrolyte for rechargeable magnesium batteries, Nano Energy. 12 (2015) 750–759, https://doi.org/10.1016/j.nanoen.2014.12.028.

[14] M.C. Lin, M. Gong, B. Lu, Y. Wu, D.Y. Wang, M. Guan, M. Angell, C. Chen, J. Yang, B.J. Hwang, H. Dai, An ultrafast rechargeable aluminium-ion battery, Nature. 520 (2015) 325–328, https://doi.org/10.1038/nature14340.

[15] Y. Liu, F. Fan, J. Wang, Y. Liu, H. Chen, K.L. Jungjohann, Y. Xu, Y. Zhu, D. Bigio, T. Zhu, C. Wang, In situ transmission electron microscopy study of electrochemical sodiation and potassiation of carbon nanofibers, Nano Lett. 14 (2014) 3445–3452, https://doi.org/10.1021/nl500970a.

[16] Z. Jian, S. Hwang, Z. Li, A.S. Hernandez, X. Wang, Z. Xing, D. Su, X. Ji, Hard-Soft Composite Carbon as a Long-Cycling and High-Rate Anode for Potassium-Ion Batteries, Adv. Funct. Mater. 27 (2017) 1–6, https://doi.org/10.1002/adfm.201700324.

[17] Z. Tai, Q. Zhang, Y. Liu, H. Liu, S. Dou, Activated carbon from the graphite with increased rate capability for the potassium ion battery, Carbon N. Y. 123 (2017) 54–61, https://doi.org/10.1016/j.carbon.2017.07.041.

[18] H. Ma, X. Qi, D. Peng, Y. Chen, D. Wei, Z. Ju, Novel Fabrication Of N / S Co-doped Hierarchically Porous Carbon For Potassium-Ion Batteries, Chemistry Select. 4 (2019) 11488–11495, https://doi.org/10.1002/slct.201903244.

[19] D. Li, X. Ren, Q. Ai, Q. Sun, L. Zhu, Y. Liu, Z. Liang, R. Peng, P. Si, J. Lou, J. Feng, L. Ci, Facile Fabrication of Nitrogen-Doped Porous Carbon as Superior Anode Material for Potassium-Ion Batteries, Adv. Energy Mater. 8 (2018) 1–9, https://doi.org/10.1002/aenm.201802386.

[20] W. Luo, J. Wan, B. Ozdemir, W. Bao, Y. Chen, J. Dai, H. Lin, Y. Xu, F. Gu, V. Barone, L. Hu, Potassium Ion Batteries with Graphitic Materials, Nano Lett. 15 (2015) 7671–7677, https://doi.org/10.1021/acs.nanolett.5b03667.

[21] Z. Xing, Y. Qi, Z. Jian, X. Ji, Polynanocrystalline Graphite: A New Carbon Anode with Superior Cycling Performance for K-Ion Batteries, ACS Appl. Mater. Interfaces. 9 (2017) 4343–4351, https://doi.org/10.1021/acsami.6b06767.

[22] L. Liu, Y. Chen, Y. Xie, P. Tao, Q. Li, C. Yan, Understanding of the Ultrastable K-Ion Storage of Carbonaceous Anode, Adv. Funct. Mater. 28 (2018) 1–9, https://doi.org/10.1002/adfm.201801989.

[23] N. Xiao, X. Zhang, C. Liu, Y. Wang, H. Li, J. Qiu, Coal-based carbon anodes for high-performance potassium-ion batteries, Carbon N. Y. 147 (2019) 574–581, https://doi.org/10.1016/j.carbon.2019.03.020.

[24] N. Cuesta, I. Cameán, A. Ramos, A.B. García, Graphitized biogas-derived carbon nanofibers as anodes for lithium-ion batteries, Electrochim. Acta. 222 (2016) 264–270, https://doi.org/10.1016/j.electacta.2016.10.170.

[25] Z. Jian, W. Luo, X. Ji, Carbon Electrodes for K-Ion Batteries, J. Am. Chem. Soc. 137 (2015) 11566–11569, https://doi.org/10.1021/jacs.5b06809.

[26] C. Gao, Q. Wang, S. Luo, Z. Wang, Y. Zhang, High performance potassium-ion battery anode based on biomorphic N- doped carbon derived from walnut septum, J. Power Sources. 415 (2019) 165–171, https://doi.org/10.1016/j.jpowsour.2019.01.073.

[27] D. Dong, Y. Zhang, Y. Xiao, T. Wang, J. Wang, W. Gao, Oxygen-enriched coal-based porous carbon under plasma-assisted MgCO3 activation as supercapacitor electrodes, Fuel. 309 (2022) 122168, https://doi.org/10.1016/j.fuel.2021.122168.

[28] J. Wang, Y. Cui, Y. Gu, H. Xu, Y. Shi, Z. Ju, Q. Zhuang, Coal-Based modified Carbon for High Performance Sodium-Ion Battery, Solid State Ionics. 368 (2021) 115701, https://doi.org/10.1016/j.ssi.2021.115701.

[29] M. Semeniuk, Z. Sarshar, S. Gezahegn, Z. Li, A. Egbedina, J. Tjong, K. Oksman, Y.H. (Cathy) Chin, M. Sain,, Catalytically transformed low energy intensive 2D-layered and single crystal-graphitic renewable carbon cathode conductors, Carbon N. Y. 183 (2021) 243–250, https://doi.org/10.1016/j.carbon.2021.06.086.

[30] C. Thambiliyagodage, L. Usgodaarachchi, Efficient removal of methylene blue by turbostratic carbon/Fe3C/Fe composite synthesized by catalytic graphitization of sucrose, Mater. Today Proc. 56 (2022) 2189–2194, https://doi.org/10.1016/j.matpr.2021.11.498.

[31] H. Li, H. Zhang, K. Li, J. Zhang, M. Sun, B. Su, Catalytic graphitization of coke carbon by iron : Understanding the evolution of carbon Structure, morphology and lattice fringes, Fuel. 279 (2020) 118531, https://doi.org/10.1016/j.fuel.2020.118531.

[32] R. Wang, G. Lu, W. Qiao, Z. Sun, H. Zhuang, J. Yu, Catalytic effect of praseodymium oxide additive on the microstructure and electrical property of graphite anode, Carbon N. Y. 95 (2015) 940–948, https://doi.org/10.1016/j.carbon.2015.09.013.

[33] J. Chen, J. Feng, L. Dong, C. Long, D. Li, Nanoporous coal via Ni-catalytic graphitization as anode materials for potassium ion battery, J. Electroanal. Chem. 862 (2020) 1–9, https://doi.org/10.1016/j.jelechem.2020.113902.

[34] F. Destyorini, Y. Irmawati, A. Hardiansyah, H. Widodo, I. Nur, D. Yahya, N. Indayaningsih, R. Yudianti, Y. Hsu, H. Uyama, Formation of nanostructured graphitic carbon from coconut waste via low-temperature catalytic graphitisation, Eng. Sci. Technol. an Int. J. 24 (2020) 514–523, https://doi.org/10.1016/j.jestch.2020.06.011.

[35] L. Tang, Q. Mao, Z. You, Z. Yao, X. Zhu, Q. Zhong, J. Xiao, Catalytic graphitization in anthracite by reduced iron particles and investigating the mechanism of catalytic transformation via molecular dynamics, Carbon N. Y. 188 (2022) 336–348, https://doi.org/10.1016/j.carbon.2021.12.031.

[36] S. Dong, Y. Song, K. Ye, J. Yan, G. Wang, K. Zhu, D. Cao, Ultra-fast, low-cost, and green regeneration of graphite anode using flash joule heating method, EcoMat. (2022) 1–10, https://doi.org/10.1002/eom2.12212.

[37] D.X. Luong, K.V. Bets, W.A. Algozeeb, M.G. Stanford, C. Kittrell, W. Chen, R. V. Salvatierra, M. Ren, E.A. McHugh, P.A. Advincula, Z. Wang, M. Bhatt, H. Guo, V. Mancevski, R. Shahsavari, B.I. Yakobson, J.M. Tour, Gram-scale bottom-up flash graphene synthesis, Nature. 577 (2020) 647–651, https://doi.org/10.1038/s41586-020-1938-0.

[38] K.M. Wyss, J.L. Beckham, W. Chen, D.X. Luong, P. Hundi, S. Raghuraman, R. Shahsavari, J.M. Tour, Converting plastic waste pyrolysis ash into flash graphene, Carbon N. Y. 174 (2021) 430–438, https://doi.org/10.1016/j.carbon.2020.12.063.

[39] A.M.A. Mohamed, D. Cao, K. Zhu, K. Chand, M. Elhefnawey, Electrochemical performances of coal-based carbon prepared by low-temperature catalytic graphitization as anode materials for potassium-ion batteries, Dig. J. Nanomater. Biostructures. 16 (2021) 1393–1399.

[40] D. Yao, C. Wang, Pyrolysis and in-line catalytic decomposition of polypropylene to carbon nanomaterials and hydrogen over Fe- and Ni-based catalysts, Appl. Energy. 265 (2020) 114819, https://doi.org/10.1016/j.apenergy.2020.114819.

[41] A.M.A. Mohamed, D. Cao, K. Chand, M. Elhefnawey, Catalytic Graphitization of Amorphous Coal at Low Temperature and its Application in Lithium-ion Batteries, 2021 IEEE 4th Int, Conf. Nanosci. Technol. ICNST 2021 (2021) 81–86, https://doi.org/10.1109/ICNST52433.2021.9509316.

[42] B. Chang, H. Yin, X. Zhang, S. Zhang, B. Yang, Chemical blowing strategy synthesis of nitrogen-rich porous graphitized carbon nanosheets: Morphology, pore structure and supercapacitor application, Chem. Eng. J. 312 (2017) 191–203, https://doi.org/10.1016/j.cej.2016.11.129.

[43] D. Dong, Y. Zhang, Y. Xiao, T. Wang, J. Wang, W. ping Pan,, Synthesis of O-doped coal-based carbon electrode materials by ultrasound-assisted bimetallic activation for application in supercapacitors, Appl. Surf. Sci. 529 (2020) 147074, https://doi.org/10.1016/j.apsusc.2020.147074.

[44] V. Paulraj, T. Saha, K. Vediappan, K. Kamala Bharathi, Synthesis and electrochemical properties of TiNb2O7 nanoparticles as an anode material for lithium ion batteries, Mater. Lett. 304 (2021), 130681, https://doi.org/10.1016/j.matlet.2021.130681.

[45] Y.K. Guruprasadagowda, M.N.K. Harish, D. Tripathy, S. Sampath, Tetrakis coumarin as efficient electrode material for rechargeable lithium ion battery, J. Electroanal. Chem. 908 (2022) 116081, https://doi.org/10.1016/j.jelechem.2022.116081.

[46] I. Cameán, P. Lavela, J.L. Tirado, A.B. García, On the electrochemical performance of anthracite-based graphite materials as anodes in lithium-ion batteries, Fuel. 89 (2010) 986–991, https://doi.org/10.1016/j.fuel.2009.06.034.

[47] K. Xia, X. Zeng, H. Zhu, J. Gong, H. Luo, Mg-doped Li2ZnTi3O8/C as high-performance anode materials for lithium-ion batteries, Vacuum. 207 (2023) 111614, https://doi.org/10.1016/j.vacuum.2022.111614.

[48] Y.J. Xu, X.H. Song, Q. Chang, X.L. Hou, Y. Sun, X.Y. Feng, X.R. Wang, M. Zhan, H. F. Xiang, Y. Yu, The regeneration of graphite anode from spent lithium-ion batteries via interface washing, New Carbon Materials. 37 (2022) 1011–1020, https://doi.org/10.1016/S1872-5805(22)60648-6.

[49] A. Ramos, I. Cameán, N. Cuesta, A.B. García, Graphitized stacked-cup carbon nanofibers as anode materials for lithium-ion batteries, Electrochim. Acta. 146 (2014) 769–775, https://doi.org/10.1016/j.electacta.2014.09.035.

[50] E. Rodríguez, I. Cameán, R. García, A.B. García, Graphitized boron-doped carbon foams: Performance as anodes in lithium-ion batteries, Electrochim. Acta. 56 (2011) 5090–5094, https://doi.org/10.1016/j.electacta.2011.03.078.

[51] I. Cameán, A.B. Garcia, Graphite materials prepared by HTT of unburned carbon from coal combustion fly ashes : Performance as anodes in lithium-ion batteries, 196 (2011) 4816–4820. https://doi.org/10.1016/j.jpowsour.2011.01.041.

[52] B. Xing, C. Zhang, Y. Cao, G. Huang, Q. Liu, C. Zhang, Z. Chen, G. Yi, L. Chen, J. Yu, Preparation of synthetic graphite from bituminous coal as anode materials for high performance lithium-ion batteries, Fuel Process. Technol. 172 (2018) 162–171, https://doi.org/10.1016/j.fuproc.2017.12.018.

[53] L. Tao, Y. Huang, Y. Zheng, X. Yang, C. Liu, M. Di, S. Larpkiattaworn, M.R. Nimlos, Z. Zheng, Porous carbon nanofiber derived from a waste biomass as anode material in lithium-ion batteries, J. Taiwan Inst. Chem. Eng. 95 (2019) 217–226, https://doi.org/10.1016/j.jtice.2018.07.005.

[54] Y. Li, R.A. Adams, A. Arora, V.G. Pol, A.M. Levine, R.J. Lee, K. Akato, A.K. Naskar, M.P. Paranthaman, Sustainable Potassium-Ion Battery Anodes Derived from Waste-Tire Rubber, J. Electrochem. Soc. 164 (2017), https://doi.org/10.1149/2.1391706jes. A1234–A1238.

[55] J. Liu, X. Yu, J. Bao, C.F. Sun, Y. Li, Carbon supported tin sulfide anodes for potassium-ion batteries, J. Phys. Chem. Solids. 153 (2021) 109992, https://doi.org/10.1016/j.jpcs.2021.109992.

[56] M. Chen, Y. Cao, C. Ma, H. Yang, A N/S/O-tridoped hard carbon network anode from mercaptan/polyurethane-acrylate resin for potassium-ion batteries, Nano Energy. 81 (2021) 105640, https://doi.org/10.1016/j.nanoen.2020.105640.

[57] D. Wang, H. Zhao, C. Zhang, H. Xu, J. Li, C. Han, Z. Li, S. Hua, W. Li, S. An, X. Qiu, Low-cost and high-rate porous carbon anode material for potassium-ion batteries, Solid State Ionics. 381 (2022) 115944, https://doi.org/10.1016/j.ssi.2022.115944.

[58] S. Yan, Q. Wang, S. Luo, Y. Zhang, X. Liu, Coal-based S hybrid self-doped porous carbon for high-performance supercapacitors and potassium-ion batteries, J. Power Sources. 461 (2020) 228151, https://doi.org/10.1016/j.jpowsour.2020.228151.

[59] Y. An, H. Fei, G. Zeng, L. Ci, B. Xi, S. Xiong, J. Feng, Commercial expanded graphite as a low – cost, long-cycling life anode for potassium – ion batteries with conventional carbonate electrolyte, J. Power Sources. 378 (2018) 66–72, https://doi.org/10.1016/j.jpowsour.2017.12.033.

[60] R.A. Adams, J.M. Syu, Y. Zhao, C.T. Lo, A. Varma, V.G. Pol, Binder-Free N- and O-Rich Carbon Nanofiber Anodes for Long Cycle Life K-Ion Batteries, ACS Appl. Mater. Interfaces. 9 (2017) 17872–17881, https://doi.org/10.1021/acsami.7b02476.